HHS Public Access

Author manuscript

Radiat Prot Dosimetry. Author manuscript; available in PMC 2017 November 28.

Published in final edited form as:

Radiat Prot Dosimetry. 2013 July ; 155(3): 300–316. doi:10.1093/rpd/nct014.

ASSESSING INTERNAL CONTAMINATION AFTER THE DETONATION OF A RADIOLOGICAL DISPERSION DEVICE USING A 2×2-INCH SODIUM IODIDE DETECTOR

S. Dewji[1,*], **N. Hertel**[1], and **A. Ansari**[2]

[1]Georgia Institute of Technology, Nuclear and Radiological Engineering Program, Atlanta, GA 30332-0405, USA

[2]Radiation Studies Branch, Centers for Disease Control and Prevention, Atlanta, GA, USA

Abstract

The detonation of a radiological dispersion device may result in a situation where individuals inhale radioactive materials and require rapid assessment of internal contamination. The feasibility of using a 2×2-inch sodium-iodide detector to determine the committed effective dose to an individual following acute inhalation of gamma-emitting radionuclides was investigated. Experimental configurations of point sources with a polymethyl methacrylate slab phantom were used to validate Monte Carlo simulations. The validated detector model was used to simulate the responses for four detector positions on six different anthropomorphic phantoms. The nuclides examined included ^{241}Am, ^{60}Co, ^{137}Cs, ^{131}I and ^{192}Ir. Biokinetic modelling was employed to determine the distributed activity in the body as a function of post-inhalation time. The simulation and biokinetic data were used to determine time-dependent count-rate values at optimal detector locations on the body for each radionuclide corresponding to a target committed effective dose (E50) value of 250 mSv.

INTRODUCTION

The terrorist threat presents numerous challenges for public health professionals. One such challenge is the rapid and effective triage of victims of a radiological dispersal device (RDD) incident. An RDD incident could leave many people both externally and internally contaminated. In such an incident, methods for assessing external contamination are better defined, whereas methods for assaying internal contamination for large populations are still deficient. *In vivo* methods are preferable to *in vitro* methods, as they facilitate the rapid screening of triage patients without cumbersome and invasive procedures, which make operations arduous in an emergency response scenario. In the former category, whole-body counters are the preferred method of assessing internal contamination in the case of gamma-emitting radionuclides. However, their use in a triage scenario is obviated by their limited availability and that they possess a greater sensitivity than required for triage. Availability restrictions are also evident for use of medical assay equipment in an emergency triage scenario following an RDD incident. Such limitations provide the inherent motivation to

*Corresponding author: shaheen.dewji@gatech.edu.

investigate whether readily available handheld instruments could be used to assess the inhaled contamination levels in a triage environment.

Sodium-iodide [NaI(Tl)] detectors are available in most university and radiation safety laboratories in major metropolitan cities. These detectors can serve as spectrometers, are robust compared with their semiconductor counterparts and are comparatively inexpensive. Such detectors consequently possess the characteristics of a fieldable detector that may be useful in a triage scenario in assessing internal contamination with gamma-emitting radionuclides.

The detector employed in this study is a Canberra 802 2×2-inch NaI(Tl) scintillation detector[(1)]. Although NaI(Tl)-integrated systems are commercially available, such systems tend to be automated and costly and lack customisability due to their task-specific design. Therefore, this study investigated the use of a standard thallium-doped 2×2-inch NaI(Tl) detector, a spectrometer in its bare form, in a field triage scenario to rapidly assess the internal contamination of a large number of individuals and prioritise them for further care. This approach assumes that each individual is free from any external contamination at the time of this screening.

The National Council on Radiation Protection and Measurements (NCRP) Report No. 161 recommends that 250 mSv be used as the target committed effective dose (E50) value for further testing and possible treatment[(2)]. In this study, action-level count rates for the 2×2-inch NaI detector corresponding to a screening target of 250 mSv committed effective dose were calculated for up to 30 d after intake.

MATERIALS AND METHODS

Simulations were employed to determine the detector count rates meeting the 250 mSv screening criteria for the distribution of inhaled radionuclides following several days after intake. Thus, the 2×2-inch NaI(Tl) detector was modelled using Los Alamos Monte Carlo N-Particle Transport Code MCNP-5[(3)] and validated via a series of benchmark measurements to ensure an accurate detector response. The overall procedure employed is outlined in the flowchart overview given in Figure 1.

Upon validation of the Monte Carlo detector model, six anthropomorphic phantoms, representative of various body types, were modelled with nuclides distributed in major organs of the body for each of the five contaminant sources under consideration. After simulation, the data were incorporated with the time-dependent biokinetic modelling, from which the threshold count-rate values for a 250 mSv committed effective dose were calculated. Further specifications and detailed analyses of the benchmarking and simulations have been explained in detail by Dewji[(4)].

Benchmark validation measurements

Slab phantom measurements—The detector models were validated by conducting measurements using a polymethyl methacrylate (PMMA) slab phantom. The slab phantom consisted of varying thicknesses of PMMA ranging in 6-mm increments from 0 to 90 mm

between the source and the detector. The PMMA sheets were followed by a source holder constructed of a 6-mm thick PMMA sheet bored with a cylindrical hole to affix the radionuclide source. The composition of PMMA (density of 1.19 g cm^{-3}) was 55.6 % carbon, 29.6 % oxygen and 14.8 % hydrogen by mass[5]. PMMA was chosen for its tissue-like attenuation behaviour with gamma rays. Thus, varying thicknesses of PMMA were used to mimic varying chest-wall thicknesses in humans. For all benchmark measurements, a 100-mm thickness of Virtual Water™ was placed behind the source holder to simulate the gamma-ray backscattering that would result from human tissue. Virtual Water™ (density of 1.03 g cm^{-3}) is composed of 8.02 % hydrogen, 67.48 % carbon, 2.14 % nitrogen, 19.91 % oxygen, 0.14 % chlorine and 2.31 % calcium by mass[6].

The detector model response was simulated for each incremental thickness of PMMA, thus replicating the slab phantom benchmark experiments. Consequently, the detector response was determined for each of the six nuclides employed in the benchmark measurements to ensure that the detector model was validated over a broad range of gamma-ray energies. The six sources investigated with the PMMA slab were ^{241}Am, ^{133}Ba, ^{60}Co, ^{137}Cs, ^{54}Mn and ^{22}Na, with assay activities given in Table 1. These nuclides were selected for validation purposes over a broad range of gamma-ray energies, whereas nuclides specific to RDD attacks are elaborated in the subsequent section.

It should be noted that the slab phantom was designed and constructed specifically for verifying and validating the MCNP model calculations and should not be considered physiological considering that a point source of radiation was emplaced in the phantom.

Detector model—Validation of the detector model resulted from the comparison of the experimental data from the slab phantoms with their simulated Monte Carlo model counterpart. The detector consisted of a standard 2×2-inch∅ NaI(Tl) scintillating crystal. The detector was modelled according to the manufacturer's design specifications[1], where the detector assembly consisted of the NaI(Tl) crystal, a photomultiplier tube and an internal magnetic/light shield, which are all hermetically sealed in an aluminium housing.

The gamma source energies and intensities for the nuclides employed in benchmark simulations corresponded to those with an emission intensity of >1 %, and were obtained from the National Nuclear Data Center through RadToolbox[7, 8].

A pulse-height tally was performed over the active region of the detector crystal to determine the pulse-height spectrum. The integrated counts in each primary photopeak region of interest (ROI) in the benchmark measurements were compared with those of the respective region in the Monte Carlo simulation. A detector response efficiency (scaling) factor was calculated for each nuclide based on the comparison for all PMMA thicknesses. Consequently, validation of the computational detector model was essential in reproducing an accurate detector response.

Measurements were accumulated as 1024-channel pulse-height spectra for the 2×2-inch detector. The MCNP pulse-height spectra were similarly binned and tallied into 1024

channels spanning a total energy range of 3.25 MeV. A rendering of the 2×2 slab phantom model with the detector using the program, VisEd program[9], is depicted in Figure 2.

For the MCNP pulse-height tally, all photoelectric interactions result in a delta function at the photon energy rather than a resolution-broadened photopeak. Thus, the Gaussian energy broadening (GEB)[3] function in MCNP was employed to attempt to simulate the detector resolution. The fit parameters for the GEB function were obtained from a fit of the full-width-at-half-maximum (FWHM) data of each of the unattenuated sources counts with the detector. The GEB function is given in Equation (1), where FWHM of the photopeak is given in MeV, E is the peak energy in MeV and a, b, c are the function fit parameters.

$$\mathrm{FWHM}=a+b\sqrt{E+cE^2}. \quad (1)$$

For the nuclides simulated in MCNP, the fit parameters in the GEB employed for the 2×2-inch detector were $a = -0.007$, $b = 0.065$ and $c = -0.179$. According to the Canberra 802-2×2 NaI(Tl) detector specifications[1], the crystal has a peak resolution of 8.5 % for the 662-keV ^{137}Cs peak, where the detector employed in the benchmark data collection yielded a peak resolution of 7.46 %, and the corresponding GEB fit had a resolution of 7.31 % at the ^{137}Cs energy.

The ROI(s) over which the counts were integrated for each radionuclide were selected to capture the nuclide's primary photopeak(s), which are summarised in Table 2. In practice, the endpoints of the ROIs were manually selected to encompass the photopeak. A sample ROI selection for both the experimental and MCNP-simulated peaks for the 662-keV peak for ^{137}Cs is shown in Figure 3.

The ROIs for ^{133}Ba and ^{60}Co consisted of the amalgamation of multiple adjacent photopeaks, which were merged into a single ROI due to their close proximity to each other, thus preserving count rates. The remaining nuclides' ROIs were singly selected peak regions, since these characteristic photopeaks were relatively isolated in energy vis-à-vis other emissions and represent high-intensity emissions. In addition, the net peak area was determined by subtracting the continuum under the peak of the ROI caused by a superimposed continuum[10].

Summation peak events were also taken into consideration when acquiring data using the PMMA slab phantoms and simulating the detector responses in MCNP. Summation events are purely a property of the incident particle flux, detector size and response and do not occur in computational modelling. Thus, for the coincidence events occurring in each of ^{60}Co, ^{137}Cs and ^{22}Na, these counts were redistributed back to the primary contributing photopeaks to attempt to preserve the number of full-energy gamma rays deposited in the detector beyond the ROI.

The results of the slab phantom benchmark measurements, in combination with the computational models of the slab phantoms, are given as energy-dependent scaling factors.

Scaling factors

The scaling factors were determined over all PMMA thicknesses for each detector and radionuclide. These scaling factors were the ratios of the simulated MCNP count rates with the detector counts in the relevant peak ROIs of the benchmark measurements. This consequently validated the detector model for each radionuclide regardless of PMMA thickness and source-detector geometry. The average ratio for each radionuclide was used as a detector-reading scaling factor applicable to other source-detector geometries.

Two nuclides used in the phantom simulations, ^{131}I and ^{192}Ir, were not included in the benchmark experiments. Therefore, their scaling factors were extrapolated via an energy-dependent linear interpolation based on the benchmark radionuclide scaling factors of adjacent energy photopeaks. The scaling factors for the benchmark measurements and those subsequently applied to the anthropomorphic phantoms are summarised in Table 2. Results were weighted towards the 35.8 mm PMMA value, which corresponds to the anteroposterior chest wall thickness of the Medical Internal Radiation Dose (MIRD) reference man (mass thickness 4.26 g cm^{-2})[11], and in order to eliminate pile-up events at smaller thicknesses. In addition, the peak efficiencies of the six validation for the 2×2-inch NaI(Tl) detector are summarised in Table 2, for an unattenuated source placed in contact with the detector surface.

Sources of error contributing to the scaling factor error in Table 2 include a predominant 3.3 % error in the checked source activity, minor contributions from statistical counting error in gross and background counts (~0.1–0.3 %), as well as error from the pulse-height tally and continuum subtraction (~0.6–1.1 %)[4]. For each nuclide, the ratios of the experimental-to-simulated values were within statistical uncertainty of each other of 1.5-standard deviations.

Upon simulation of the appropriate measurements and obtaining a constant-averaged scaling factor from the detector response, the detector model was validated for use with the anthropomorphic phantoms.

Anthropomorphic phantom models

The computational phantom models employed were based on the MIRD anthropomorphic phantoms[11]. The MIRD phantoms are based on the reference male and female body types, and are based on the mathematical phantoms, which were coded into MCNP[12] using the ICRP Publication 23 recommendations[13]. The development of the adipose phantoms was an extension of these models[14], and resulted in the creation of three additional adult phantoms: adipose male, adipose female and post-menopausal adipose female. These phantoms have been modified with the addition of a 2-mm layer of skin tissue, an oesophagus and a walled colon[15]. An androgynous 10-y-old child phantom was constructed using BodyBuilder[16]. Thus, a total of six phantoms—five adult (two reference, three adipose) and a child phantom—were employed in this simulation.

The adult phantoms can be characterised according to their height, body mass index (BMI) and the adipose tissue mass. The BMI is calculated as the ratio of the weight (kg) to the

square of the height (m^2). The physical characteristics of the six phantoms are summarised in Table 3.

The radionuclides included in this study were ^{241}Am, ^{60}Co, ^{137}Cs, ^{131}I and ^{192}Ir. These were radio-nuclides of 'greatest concern' as identified by the Nuclear Regulatory Commission and Department of Energy Working Group on RDDs[17]. Each phantom was simulated with a unit source of each radionuclide distributed uniformly in each organ, from which the detector response was determined for the anthropomorphic phantoms.

The validated MCNP detector model once again employed a pulse-height tally to simulate the detector response at various locations on the surface of the anthropomorphic phantoms. The detector model was placed at four locations about the phantom: Anterior neck, anterior and posterior right upper torso and lateral left thigh. Each of these locations was assessed to determine which location would yield an optimal detection count rate. All the four locations were employed using the reference male phantom, though the anterior upper-right torso position was omitted from the remainder of the phantoms due to adipose/breast tissue attenuation at this location with the reference female, adipose male, adipose female and post-menopausal adipose female phantoms.

The count rates at the four detector locations were simulated and the optimal count-rate location for each of the five radionuclides was chosen for use in triaging. The torso locations over the right lung were selected, as the three-lobed right lung is larger than the two-lobed left lung. Posterior and anterior locations were selected due to attenuation effects of breast tissue and fat. The neck was selected, since ^{131}I is a well-known thyroid-seeker. Finally, the thigh location was selected, as it represents a large and fleshy muscular region where body tissue seeking nuclides may migrate. In addition, significant bone volume is present in the thigh from the femur and lower pelvis, where soluble forms of radionuclides, such as ^{241}Am, can be significantly deposited significantly in bone, even following early exposure. A VisEd[9] representation of these detector placement locations is displayed in Figure 4.

Biokinetic modelling

Biokinetic modelling was employed to simulate the distribution of radionuclides through the body as a function of time. The source organ distribution used to represent inhaled source contamination was determined using the Dose and Risk Calculation (DCAL) software[18].

The DCAL software implements the ICRP Publication 66 respiratory biokinetics to determine the retention factors for a given radionuclide inhalation class in the body as a function of time[19]. Dosimetric calculations in DCAL are conducted via three main steps[18]: first, the calculation of the time-dependent activity for the parent nuclide and its progeny present in anatomical (source) regions in the body. Second, for all source and target regions, specific effective energy (SEE) values are calculated as a function of these source and target regions. In the calculation of SEE, dose rates in the target region are given per unit of activity in the source. Finally, based on the first two steps, dose (or dose equivalent) rates are calculated. The culmination of these three calculations provides dose coefficients, providing the integrated organ dose (or dose equivalent) per unit of activity intake.

DCAL was used to determine the accumulated amount of radionuclide present in an organ after a given time—thus tracking the biological/metabolic and radiological decay effects. The activity calculation module is a component in the DCAL package that calculates the time-dependent activity in various body compartments for a given parent radionuclide.

For each of the five radionuclides under investigation, DCAL was executed using ICRP Publication 72 default inhalation types[20]. Each nuclide was specified as inhalation from an environmental source (vis-à-vis an occupational source) as the intake pathway. A default of 1 μm was used as the particle's activity mean aerodynamic diameter[18]. The lung absorption type (slow [S], moderate [M], fast [F]) corresponded to the speed with which the particulate nuclide is absorbed in the lungs, and corresponded to ICRP Publication 72-recommended defaults[18, 20]. The default lung absorption type for ^{137}Cs and ^{131}I is fast, whereas ^{60}Co and ^{241}Am have a moderate uptake speed. Since a default lung absorption type was not specified for ^{192}Ir, a moderate uptake was assumed[21]. A summary of the default inhalation types and environmental inhalation dose coefficients for an adult and child are given in Table 4.

The fraction of retention only for the significantly contributing compartments was determined for each of the five radionuclides under investigation over a period of 30 d. The exathoracic compartments, ET1 (anterior nose) and ET2 (posterior nasal passage, mouth, larynx, pharynx), from the ICRP Publication 66 respiratory tract model[19] were subtracted from the retained lung fraction calculated in DCAL. This rationale is based on the premise that most of the contamination from these passages will be removed prior to screening.

The activity retained in the blood calculated by DCAL was distributed among the body organs based on the blood distributions given in ICRP Publication 89[22, 23]. The remainder of the blood not allocated to specific organs was distributed uniformly in the body tissue.

The DCAL output calculates retention as a function of the biological metabolic processes, as well as the nuclide's half-life. The DCAL results showing fraction retained in the body of the inhaled activity for all nuclides are displayed in Figures 5–9.

Folding biokinetic with MCNP data

In the MCNP model of the anthropomorphic phantoms, the source contribution tally modifier was employed to determine the source organ contribution for each source particle that reaches the detector. Once the MCNP tally data for each source compartment at each detector location was folded with the DCAL biokinetic data, the resulting output was given in counts per Becquerel (Bq) of intake activity. Applying the dose conversion factors at the 250 mSv action level yields a final result in count rate (cpm) per 250 mSv intake.

Summing the contributions from each source organ from the MCNP pulse-height tally, in conjunction with the biokinetic modelling—which contributes the fractional organ contribution as a function of time per Bq of intake—yields a total count rate from detector per Bq of intake (cpm Bq^{-1}). Finally, by applying dose conversion coefficients for the inhaled activity that would lead to a committed effective dose of 250 mSv, the count rate per

250 mSv was obtained (cpm 250 mSv^{-1}). Each detector location was tallied for each of ^{241}Am, ^{60}Co, ^{137}Cs, ^{131}I and ^{192}Ir (full results available in Dewji[4]).

Detection count-rate thresholds

Since radioactivity count rates tend to fluctuate statistically, a minimum threshold must be established to discern a lower limit of detection with confidence above background levels. The decision level (DL) was calculated to determine whether or not a sample was detectable above background levels with a pre-established confidence interval[24, 25]. This estimate, based on background measurements, does not serve as a decision-making mechanism, but rather describes the detection capability and sensitivity of the system. Thus, a DL must be established to determine the net count rate of a sample above background with a pre-established confidence interval. This DL takes the form of Equation (2).

$$\mathrm{DL}=1.645\sqrt{R_{\mathrm{b}}\left(\frac{1}{t_{\mathrm{b}}}+\frac{1}{t_{\mathrm{g}}}\right)}. \quad (2)$$

In Equation (2), R_b is the background count rate (cpm), t_b is the background acquisition time (min) and t_g is the sample acquisition time (min). For the background data taken with the NaI(Tl) detector during the slab phantom measurements, the DL was calculated based on Equation (2), and is summarised for various sample acquisition times in Table 5. However, as defined by the specific environmental background data in which the detector is employed, a count rate of at least 44.5 cpm (from ^{241}Am ROI data) above background is required for the 2×2 detector to justify the presence of true activity within 95 % confidence intervals, potentially limiting the detection capabilities of ^{241}Am. This count rate was calculated as a function of the background spectrum; thus, the minimum detection limit will vary according to the background environment in which the patient is being assessed. In a high contamination environment, it is possible that the threshold to detect ^{241}Am is increased, making it virtually undetectable. However, it can be reasonably expected that screening for internal contamination will not take place in a highly contaminated environment.

For ^{137}Cs, ^{60}Co, ^{131}I and ^{192}Ir, a count time of 1 min easily supersedes the DLs, based on the facility background in which validation data were acquired (Table 5). It would appear that a longer acquisition time for ^{241}Am should be employed, although the triage count rates are still above the DL until 20 d after the intake. It is expected that triage operators would acquire their own site-specific background and use the net counts summarised in Tables 6 and 7 to make triaging decisions. In essence, this is only required for ^{241}Am assay.

RESULTS AND DISCUSSION

The optimal location for detector placement in the event of a minimum uptake of 250 mSv committed effective dose is dependent on the nuclide inhaled. Overall, the location yielding a sufficient, if not optimal, detectable count rate is the posterior right lung. As will be discussed, this was the case for all nuclides, with the exception of ^{131}I, where the neck

location had proved optimal or very close to optimal for all phantoms, as ^{131}I is a thyroid-seeker.

Although body type plays a prominent role in determining detector response and count rate, it must also be noted that the contaminant nuclide under consideration also contributes to the subsequent detector response by its mode of accumulation in the body. For phantoms with the detector optimally located at the posterior right torso position, the child phantom tended to yield the highest count rate, due to a thin wall and comparatively less attenuation. In addition, the higher count rate in the child phantom is also due to the fact the source organs are smaller and more compact than those of the adult phantoms, consequently yielding increased detection efficiency.

Conversely, the adipose phantoms tended to yield lower count rates, due to increased attenuation by a larger chest wall of breast tissue and fat. The adipose male phantom yielded the lowest count rates for all but ^{137}Cs, where the post-menopausal female yielded the most conservative count rates. Thus, if a single phantom was to be used for triage assessment, the adipose male phantom data would provide the most conservative count rates among all adult phantoms. Given that it is often difficult to classify adult body-types in a mass triage scenario, the adipose male count-rate data for the detector placed over the posterior right lung summarised in Table 6 could be used to triage all adult patients. Note that the post-menopausal female data for ^{137}Cs are employed in Table 6, as it was more conservative than the adipose male in the case of this one nuclide. The count-rate data for the detector placed over the posterior right lung for an uptake of 250 mSv in the child phantom are summarised in Table 7.

The behaviour of ^{137}Cs shows count rates closely distributed when comparing the adult phantoms in Figure 10. The optimal detector location for ^{137}Cs occurs when placed over the lung location, even though the source of these counts results from contaminant movement through the visceral body tissue, not lung retention (fast absorption type), as seen in Figure 7. In assessing ^{137}Cs levels in all phantoms, the lateral left thigh location yielded counts on the same order of magnitude as the posterior lung data. Consequently, the thigh location would as a suitable alternative location to the lung for assay ~1 d following initial contamination, once the nuclide has migrated. The thigh represents a large form of muscle tissue, and given that ^{137}Cs is a fast-absorbing nuclide targeting the body tissue, it is reasonable to conclude that the thigh would be a suitable alternative for detection.

In the cases of ^{60}Co and ^{192}Ir, both nuclides have moderate lung absorption types. As seen in Figures 11 and 12, respectively, both ^{60}Co and ^{192}Ir tend to receive most of their counts due to contributions from where these nuclides tend to accumulate: the lungs, body tissue and visceral organs.

In the case of detecting ^{131}I with the detector, its optimal counting location is when placed over the anterior neck, where source counts originate from the thyroid (Figure 8). Yet, the child phantom yields the lowest count rate (Figure 13) because ^{131}I is rapidly taken up by the thyroid gland and proceeds at a higher metabolic rate in a child. Additionally, ^{131}I has a short radiological half-life of 8.04 d[8]. The neck was determined to be the optimal location

for the detection of ^{131}I, though employing the posterior right torso position would also yield sufficient counts for assaying contamination and providing a consistent body location for all nuclides for first responders during triage.

For the five contaminant nuclides, the majority of the counts tend to originate from either the lungs or body tissue. The two distinctively detectable nuclides with moderate lung absorptions, ^{60}Co and ^{192}Ir, have a majority of their counts originating from the lungs. Conversely, the nuclides with fast lung absorptions, ^{131}I and ^{137}Cs, have a majority of counts originating from the body tissue (with the exception of the thyroid uptake of ^{131}I). This is due to the fact that the fast-uptake nuclides more rapidly clear the lungs into the body, while the moderate-uptake nuclides linger for longer in the lungs. As previously mentioned with ^{137}Cs, even though the lung and neck locations yield optimal count rates, this is not due to retention in the lungs, but due to counts from the inhaled contaminant having metabolised in the body tissue and emitted gammas over these large areas of tissue.

As noted earlier, summation events are not simulated in MCNP. Thus, the simulated detector threshold count rates, notably for ^{60}Co and ^{137}Cs, do not account for subsequent summation events that occur beyond the ROI in actual NaI(Tl) detectors. Based on the PMMA data, these MCNP phantom data were each fitted empirically to yield a relationship between the count rate in the ROI and the fraction of detected counts (including summation events) occurring in the ROI. This empirical redistribution accounted for the fact that at high incidence count rates, a fraction of these counts will occur in the sum peak. This empirical correction was applied to the detector response count-rate thresholds obtained from the MCNP phantom models, in order to provide realistic detector responses.

The lowest count rate from all the sampled nuclides originated from ^{241}Am. The easily attenuated low-energy gamma rays (59.5 keV) permit only a small fraction of the gamma rays to reach the detector, thus resulting in a count rate per 250 mSv intake that is many orders of magnitude lower than those of the other nuclides. Most of the committed effective dose for ^{241}Am is due to the fact that it is predominantly an alpha emitter.

The count rates for ^{241}Am were detectable above the background threshold for all phantoms, but the count rates for the adipose male (Figure 14) closely approach the 95 % statistical confidence detection limit calculated in Table 5. Additionally, as seen in Table 4, the intake quantities of ^{241}Am, corresponding to the 250 mSv screening criterion in both adults and children, are approximately four orders of magnitude lower than those of the other nuclides. In the absence of the ability to detect low activities of ^{241}Am, it is quite possible that a considerable dose can be delivered by the time the detector can definitively detect an adequate count rate above the background detection limit. In order to adequately detect ^{241}Am, an assay acquisition time well exceeding 10 min will be required. Therefore, ^{241}Am is considered tentatively detectable by the NaI(Tl) detector for inhaled contamination (Figure 14), best under low background circumstances with higher acquisition times. Urine bioassay, if feasible, will provide a more reliable method of screening for ^{241}Am.

CONCLUSION

For the purpose of triage, the 2×2 Na(Tl) detector is capable of assaying individuals having inhaled gamma-emitting radionuclides after an RDD incident. The detector is capable of definitively assaying the four of the five nuclides investigated: ^{60}Co, ^{137}Cs, ^{131}I and ^{192}Ir at levels corresponding to the 250 mSv screening criterion, with a counting time of 1 min. However, ^{241}Am closely approaches minimum detection thresholds and consequently may not be detected in situations of short counting times and/or in the presence of elevated background levels.

Given the complex nature of the instrument and the calibration required, it is strongly recommended that trained personnel with experience using sodium-iodide detectors conduct the initial instrument set-up and provide supervision during the screening process. The detector itself is not hand-portable and requires the set-up of modules, energy calibrations and ROI determination. Therefore, only with the assistance of technical personnel experienced in operating sodium-iodide detectors is it feasible to use this instrument effectively to triage potentially contaminated people. The method described in this study provides an additional tool for triage and prioritisation of people when a large population needs rapid screening.

Acknowledgments

The authors thank Dr Eric Burgett, Dr Ryan Manger, Mr Michael Bellamy and Ms Randahl Palmer for their technical assistance on this project.

FUNDING

This work was supported by the Centers for Disease Control and Prevention, Radiation Studies Branch through TKCIS. The findings and conclusions in this report are those of the authors and do not necessarily represent the official position of the Centers for Disease Control and Prevention.

References

1. Canberra Industries. Canberra scintillation detectors—model 802. Canberra Industries Inc; 2003. Available on http://www.canberra.com/products/detectors/pdf/Model-802-SS-CSP0232.pdf
2. National council on radiation protection and measurements management of persons contaminated with radionuclides: handbook. NCRP. 2008; 161:56–61. 158–160.
3. X-5 Monte Carlo Team. Los Alamos National Laboratory/LA-CP-03-0245. 2003. MCNP a general Monte Carlo N-particle transport code version 5, volumes I, II, and III: user's guide.
4. Dewji, SA. Assessing internal contamination after a radiological dispersion device event using a 2×2-inch sodium-iodide detector. Master of Science Thesis in Nuclear and Radiological Engineering. Georgia Institute of Technology; 2009. Available on http://hdl.handle.net/1853/28092
5. National Institute of Standards and Technology. NIST standard reference materials. 2009. Available on http://www.nist.gov/srd/materials.cfm
6. Wang Z, Hertel N. Determination of dosimetric characteristics of OptiSeed a plastic brachy-therapy Pd-103 source. Appl Radiat Isot. 2005; 63:311–321. [PubMed: 15964196]
7. National Nuclear Data Center. Nuclear wallet cards. 2012. Available on http://www.nndc.bnl.gov/
8. Eckerman, KF., Sjoreen, AL. Radiological toolbox. Oak Ridge National Laboratory; 2003. ORNL/TM-2004/27R1Available on https://forms.nrc.gov/aboutnrc/regulatory/research/manual.pdf
9. Schwarz, RA. MCNP visual editor. Los Alamos National Laboratory; 2005.
10. Knoll, GF. Radiation Detection and Measurement. Wiley; 2000.

11. Eckerman, KF., Cristy, M., Ryman, JC. ORNL mathematical phantom series. National Laboratory; 1996.
12. Tanner, JE. Current dose studies on effective neutron dose equivalent. Proceedings of Eleventh DOE Workshop on Personnel Neutron Dosimetry; Las Vegas, NV. 1991. p. 173-191.
13. International Commission on Radiological Protection. ICRP Publication 23, Ann ICRP. Vol. 4. Pergamon Press; 1980. Report of the task group on reference male (1975).
14. Simpkins, RW. Neutron organ dose and the influence of adipose tissue. A Thesis Presented to the Faculty. Georgia Institute of Technology; 2003. Available on http://hdl.handle.net/1853/18959
15. Burns, KA. Monte Carlo Simulations for Homeland Security Using Simulations for Homeland Security Using Anthropomorphic Phantoms: Master of Science Thesis in Nuclear and Radiological Engineering. Georgia Institute of Technology; 2008. Available on http://hdl.handle.net/1853/22573
16. Van Riper, KA. Bodybuilder. White Rock Science; 2004.
17. DOE/NRC Interagency Working Group on Radiological Dispersal Devices. Report to the Nuclear Regulatory Commission and the Secretary of Energy, Nuclear Regulatory Commission. 2003. Radiological dispersal devices: an initial study to identify radioactive materials of greatest concern and approaches to their tracking, tagging, and disposition.
18. Eckerman, KF., Leggett, RW., Cristy, M., Nelson, CB., Ryman, JC., Sjoreen, AL., Ward, RC. Dose and risk calculation software. Oak Ridge National Laboratory; 2006. ORNL/TM-2001/190
19. International Commission on Radiological Protection. ICRP Publication 66, Ann ICRP. Vol. 24. Pergamon Press; 1994. Human respiratory tract model for radiological protection.
20. International Commission on Radiological Protection. ICRP Publication 72, Ann ICRP. Vol. 26. Pergamon Press; 1996. Age-dependent dose to members of the public from intake of radionuclides, Part 5 compilation of ingestion and inhalation dose coefficients.
21. Scarboro, SB. A Thesis Presented to the Faculty. Georgia Institute of Technology; 2008. The use of a thyroid uptake system for assaying internal contamination following a radioactive dispersal event. Available on http://hdl.handle.net/1853/22639
22. International Commission on Radiological Protection. ICRP Publication 89, Ann ICRP. Vol. 32. Pergamon Press; 2002. Basic anatomical and physiological data for use in radiological protection: reference values.
23. Freibert, EJ. Assessing Internal Contamination Levels for Fission Product Inhalation Using a Portal Monitor: Master of Science Thesis in Nuclear and Radiological Engineering. Georgia Institute of Technology; 2010. Available on http://hdl.handle.net/1853/37184
24. ISO 11929. Determination of the characteristic limits (decision threshold, detection limit and limits of the confidence interval) for measurements of ionizing radiation e fundamentals and application. ISO; 2010.
25. Strom, DJ. False alarms, true alarms, and statistics: correct usage of decision level and minimum detectable amount. Proceedings of Health Physics Society Annual Meeting, Continuing Education Lecture; Minneapolis, MN. 15 July (1998);

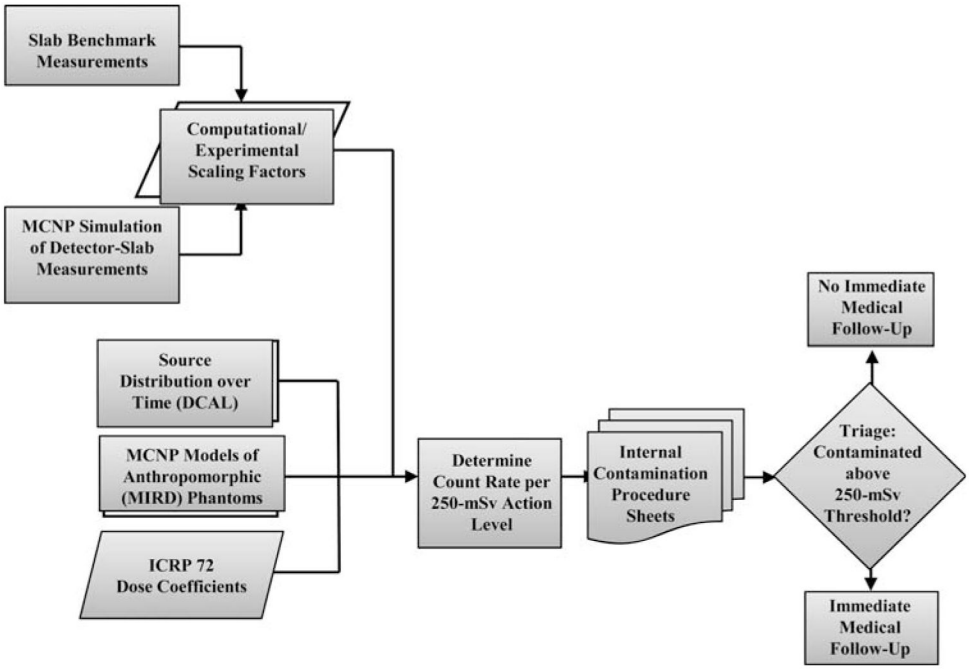

Figure 1.

Methodology for determining inhalation contamination triage levels using a 2×2-inch NaI(Tl) detector.

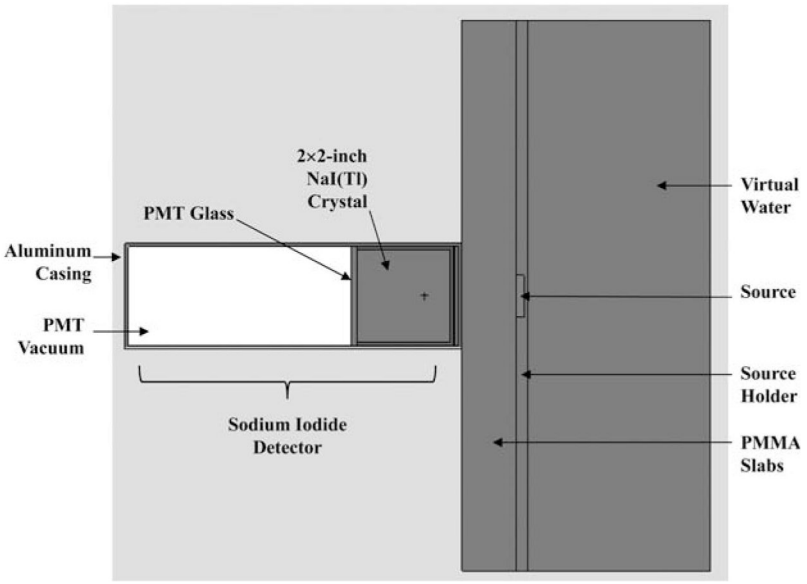

Figure 2.
VisEd representation of PMMA slab phantom model and NaI(Tl) detector.

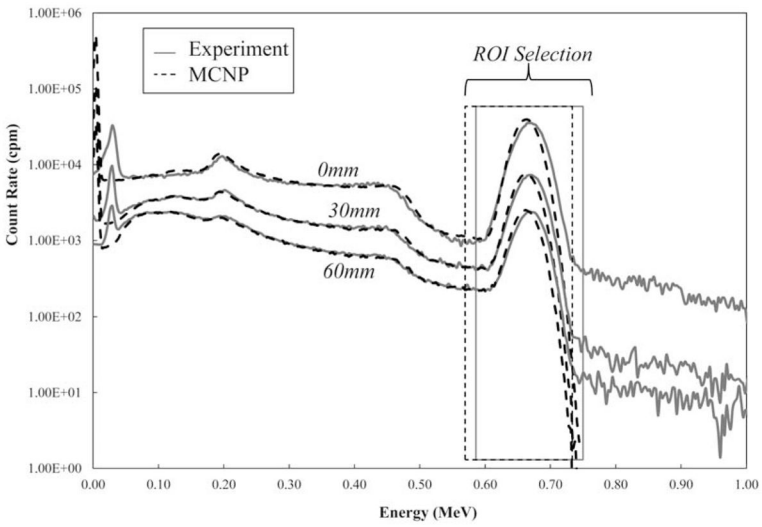

Figure 3.
Sample 'ROI' comparison for ^{137}Cs experimental slab data and MCNP simulation model for varying thicknesses of PMMA.

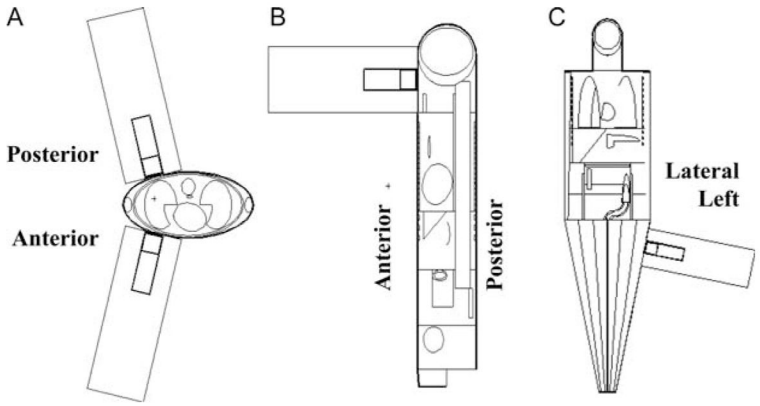

Figure 4.

Detector placement locations on anthropomorphic phantom: (**A**) anterior and posterior right upper torso; (**B**) anterior neck; (**C**) lateral left thigh.

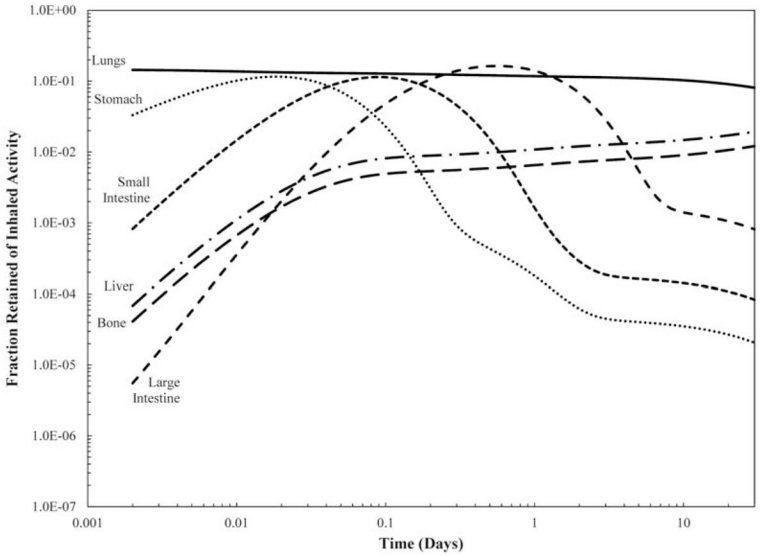

Figure 5.
Retention of ^{241}Am (moderate) in major contributing compartments over a 30-d period.

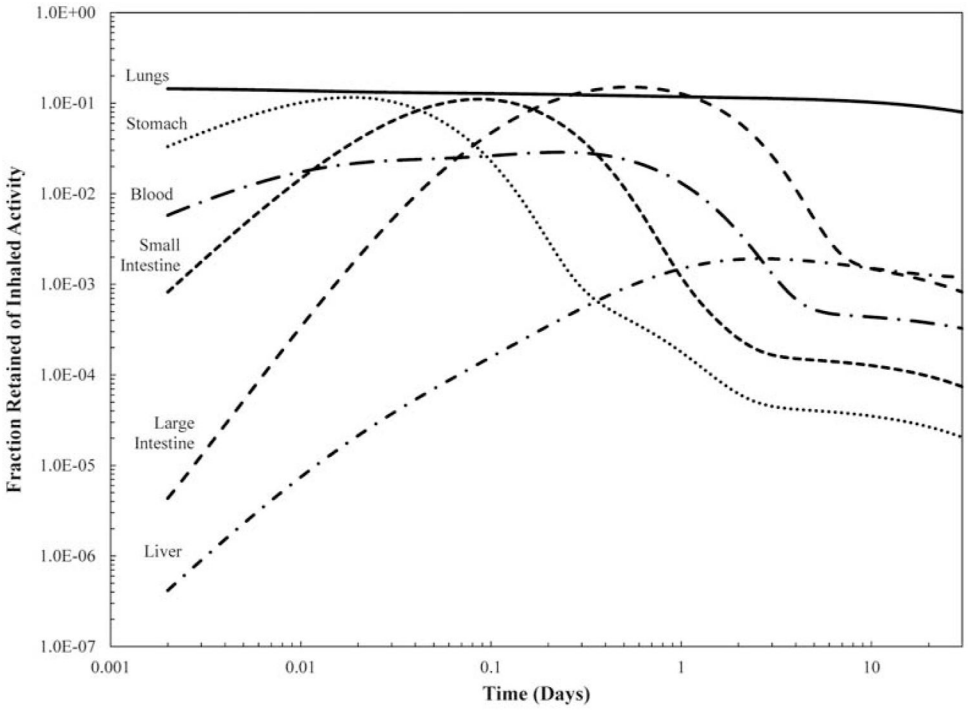

Figure 6.
Retention of ^{60}Co (moderate) in major contributing compartments over a 30-d period.

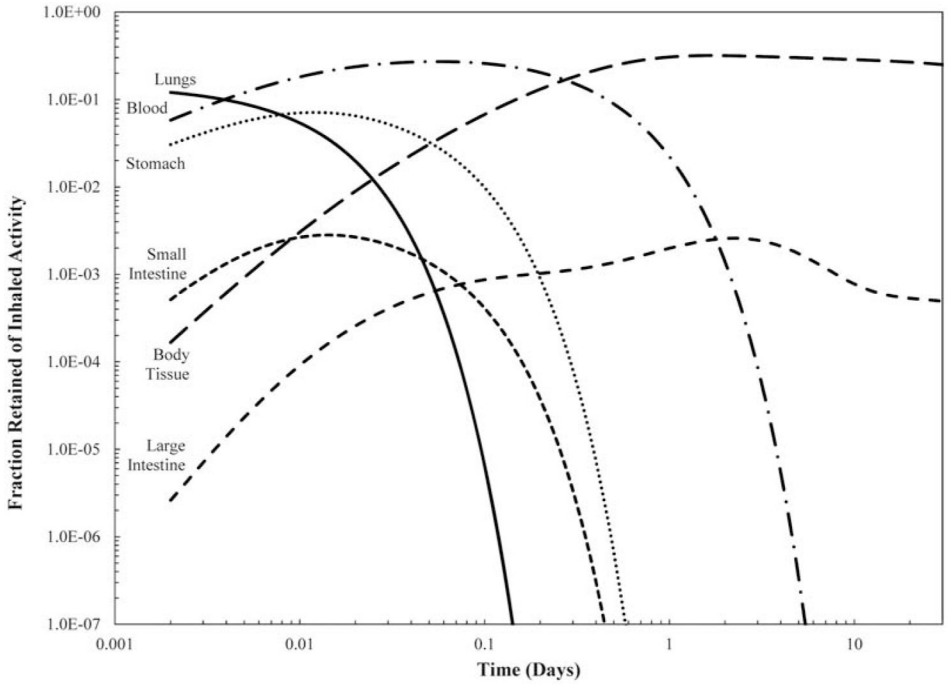

Figure 7.
Retention of ^{137}Cs (fast) in major contributing compartments over a 30-d period.

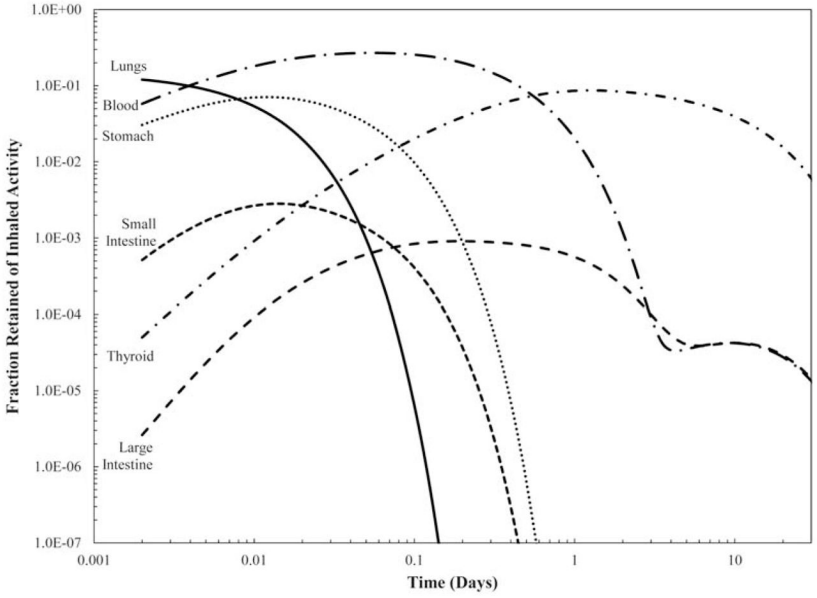

Figure 8.
Retention of ^{131}I (fast) in major contributing compartments over a 30-d period.

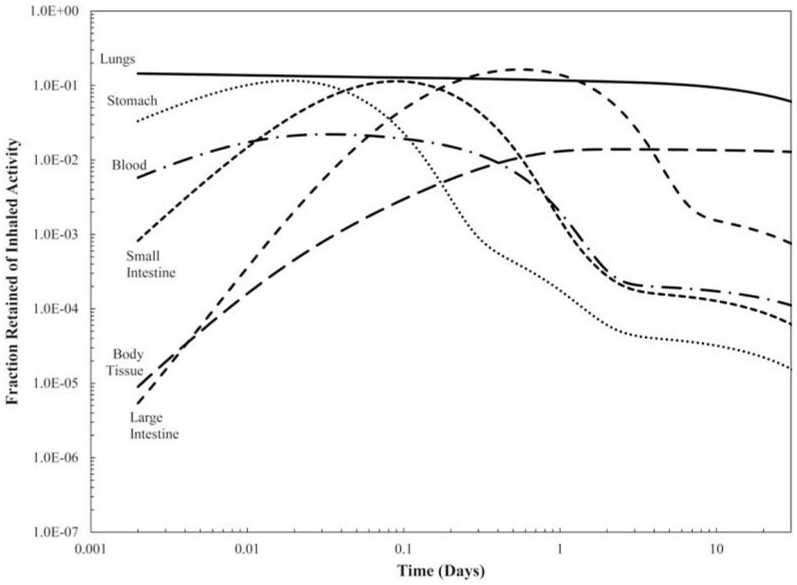

Figure 9.
Retention of ^{192}Ir (moderate) in major contributing compartments over a 30-d period.

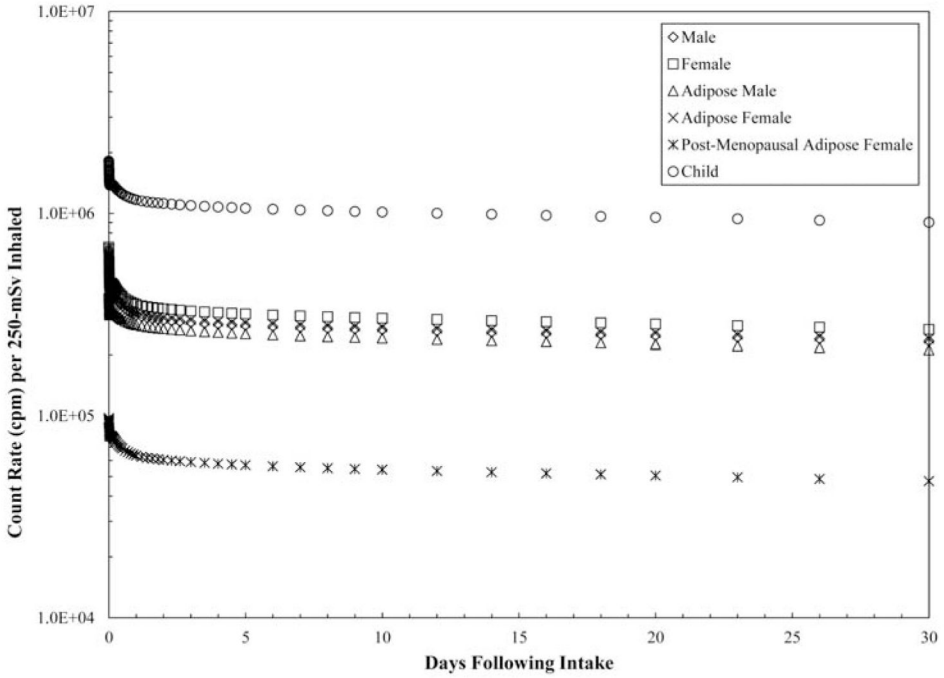

Figure 10.
Comparison of count rate per phantom for ^{137}Cs at posterior right lung position.

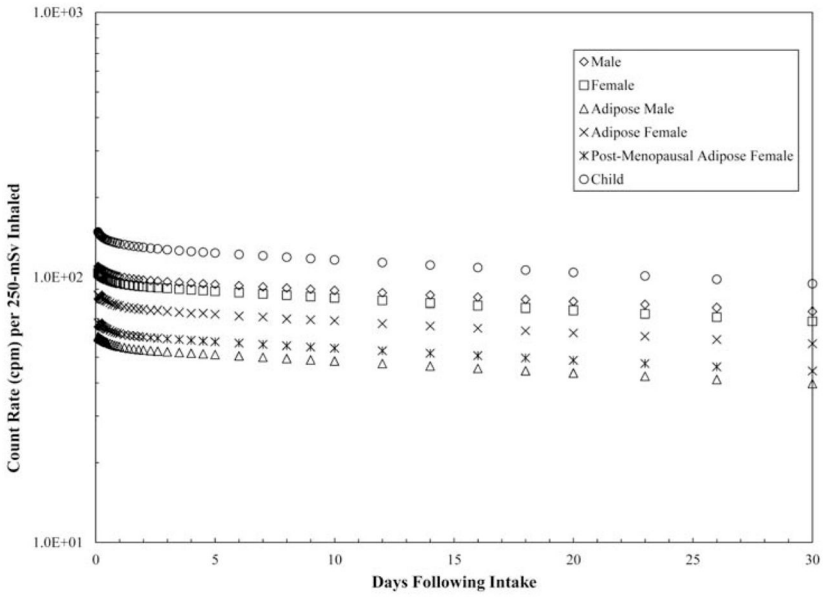

Figure 11.
Comparison of count rate per phantom for ^{60}Co at posterior right lung position.

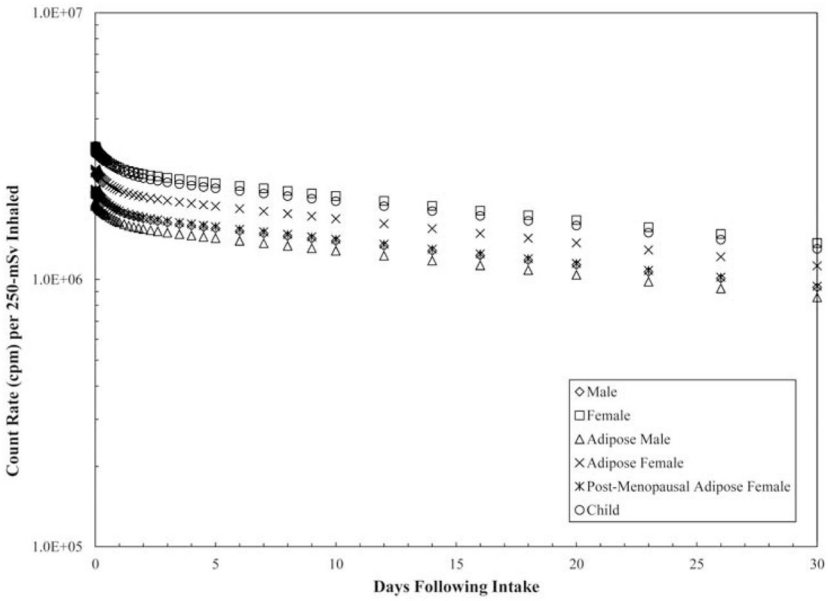

Figure 12.
Comparison of count rate per phantom for ^{192}Ir at posterior right lung position.

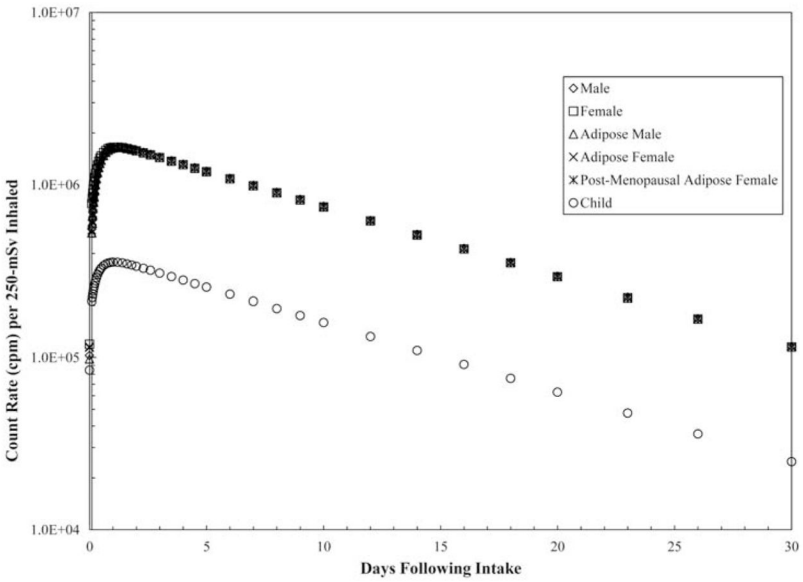

Figure 13.
Comparison of count rate per phantom for ^{131}I at anterior neck position.

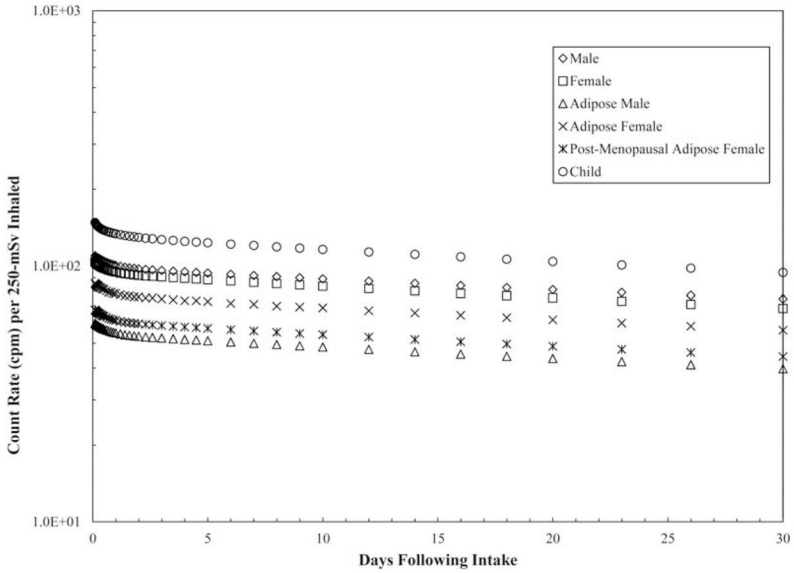

Figure 14.
Comparison of count rate per phantom for ^{241}Am at posterior right lung position.

Table 1

Activities of sources employed in benchmark validation experiments.

Nuclide	Assay date (mm/dd/yy)	Initial activity (μCi)[a]	Half-life (y)	Activity during slab phantom validation (μCi)
^{241}Am	12/09/05	7.50	432	7.48
^{133}Ba	12/09/05	5.20	10.7	4.50
^{22}Na	12/09/05	5.10	5.27	4.02
^{137}Cs	12/09/05	4.90	30.0	4.70
^{54}Mn	12/09/05	5.00	0.86	1.15
^{60}Co	12/09/05	5.00	2.60	3.09

[a]Sources employed are NIST-traceable with an assay error of 3.3 %.

Table 2

Nuclide gamma-ray photopeak energies and scaling factors radionuclide sources.

Nuclide	Peak energy (keV)	Emission intensity[a]	Peak efficiency (ROI cps dps^{-1})[b]	Scaling factor ($\pm\sigma$)
^{241}Amc	59.5	0.357	8.50 %	1.00±0.05
^{133}Bad	276.4	0.071	3.43 %	0.96±0.04
	302.9	0.184		
	356.0	0.622		
^{22}Na	511.0	1.798	4.40 %	0.92±0.05
	1274.5	0.999	1.75 %	0.97±0.05
^{137}Cs[c]	661.7	0.851	6.47 %	0.89±0.04
^{54}Mn	834.8	0.999	4.87 %	0.93±0.02
^{60}Co[c,d]	1173.2	0.998	2.31 %	0.85±0.03
	1332.5	0.999		
^{131}I[c,e]	364.5	0.817		0.96
^{192}Ir[c,d,e]	295.9	0.287		0.95
	308.4	0.300		
	316.5	0.828		

[a] Values obtained from National Nuclear Data Center(7).

[b] Peak efficiency for unattenuated source on detector surface.

[c] Employed in anthropomorphic phantom simulations for ‘nuclides of greatest interest’ in RDD scenario.

[d] Combined ROI for multiple adjacent photopeaks.

[e] Interpolated values from neighbouring photopeak scaling factors.

Table 3

Anthropomorphic phantom physical characteristics.

Phantom	Height (cm)	Mass (kg)	BMI
Reference male	179	73.1	23
Reference female	168	56.5	20
Adipose male	179	93.7	30
Adipose female	168	73.9	26
Post-menopausal adipose female	168	85.9	30
10-y old androgynous child	140	32.7	N/A

Table 4

ICRP Publication 72 environmental inhalation dose coefficients[20].

Nuclide	Default lung absorption type	Adult inhalation coefficient (Bq 250 mSv^{-1} intake)	Child inhalation coefficient (Bq 250 mSv^{-1} intake)
^{241}Am	M	5.95×10^{3}	6.25×10^{3}
^{60}Co	M	2.50×10^{7}	1.67×10^{7}
^{137}Cs	F	5.43×10^{7}	1.25×10^{8}
^{131}I	F	3.38×10^{7}	1.32×10^{7}
^{192}Ir	M	4.81×10^{7}	3.29×10^{7}

Table 5

Minimum detectable count rates for various counting times for 2×2-NaI(Tl) detector.

Nuclide	Background count rate in ROI (cpm)	DL (above background) for various acquisition times (cpm)		
		1 min	5 min	10 min
^{241}Am	728.2	44.5	20.1	14.4
^{60}Co	969.1	51.4	23.2	16.6
^{137}Cs	542.8	38.4	17.4	12.5
^{131}I	1784.8	69.7	31.5	22.6
^{192}Ir	3701.5	100.4	45.5	32.5

Table 6

Adult triage screening levels per 250 mSv intake for 2×2 NaI(Tl) detector on posterior right lung location[a].

Adult	Action level for inhaled contamination (cpm 250 mSv^{-1})				
Time (days)	^{241}Am	^{60}Co	^{137}Cs[b]	^{131}I	^{192}Ir
0.0	6.40×10^{1}	2.27×10^{5}	9.65×10^{4}	4.75×10^{5}	1.88×10^{6}
0.2	5.88×10^{1}	2.28×10^{5}	7.63×10^{4}	2.46×10^{5}	1.82×10^{6}
0.5	5.68×10^{1}	2.21×10^{5}	6.87×10^{4}	1.23×10^{5}	1.73×10^{6}
1.0	5.48×10^{1}	2.11×10^{5}	6.36×10^{4}	5.20×10^{4}	1.64×10^{6}
2.0	5.32×10^{1}	2.01×10^{5}	6.05×10^{4}	2.93×10^{4}	1.54×10^{6}
3.0	5.24×10^{1}	1.96×10^{5}	5.90×10^{4}	2.61×10^{4}	1.50×10^{6}
4.0	5.17×10^{1}	1.93×10^{5}	5.78×10^{4}	2.42×10^{4}	1.46×10^{6}
5.0	5.11×10^{1}	1.91×10^{5}	5.69×10^{4}	2.24×10^{4}	1.43×10^{6}
6.0	5.05×10^{1}	1.89×10^{5}	5.62×10^{4}	2.08×10^{4}	1.39×10^{6}
7.0	5.00×10^{1}	1.87×10^{5}	5.55×10^{4}	1.92×10^{4}	1.36×10^{6}
8.0	4.94×10^{1}	1.85×10^{5}	5.50×10^{4}	1.78×10^{4}	1.34×10^{6}
9.0	4.89×10^{1}	1.82×10^{5}	5.45×10^{4}	1.64×10^{4}	1.31×10^{6}
10.0	4.83×10^{1}	1.81×10^{5}	5.41×10^{4}	1.52×10^{4}	1.28×10^{6}
20.0	4.36×10^{1}	1.63×10^{5}	5.05×10^{4}	6.56×10^{4}	1.04×10^{6}
30.0	3.98×10^{1}	1.48×10^{5}	4.74×10^{4}	2.73×10^{4}	8.56×10^{5}

[a] Count rates provided are independent of background. Since background is site dependent, it will need to be independently acquired and subtracted from gross count rates to obtain the triage threshold values.

[b] To include a measure of conservatism, all data except ^{137}Cs are from adipose male phantom. The ^{137}Cs data are from post-menopausal female phantom.

Table 7

Child triage screening levels per 250 mSv intake for 2×2 NaI(Tl) detector on posterior right lung location.

Child	Action level for inhaled contamination (cpm 250 mSv^{-1})				
Time (d)	^{241}Am	^{60}Co	^{137}Cs	^{131}I	^{192}Ir
0.0	1.57×10^{2}	3.36×10^{5}	1.82×10^{6}	4.39×10^{5}	2.97×10^{6}
0.2	1.44×10^{2}	3.39×10^{5}	1.36×10^{6}	2.24×10^{5}	2.94×10^{6}
0.5	1.38×10^{2}	3.35×10^{5}	1.25×10^{6}	1.23×10^{5}	2.77×10^{6}
1.0	1.34×10^{2}	3.27×10^{5}	1.17×10^{6}	6.55×10^{4}	2.58×10^{6}
2.0	1.29×10^{2}	3.18×10^{5}	1.12×10^{6}	4.51×10^{4}	2.40×10^{6}
3.0	1.27×10^{2}	3.13×10^{5}	1.09×10^{6}	4.07×10^{4}	2.31×10^{6}
4.0	1.25×10^{2}	3.10×10^{5}	1.07×10^{6}	3.73×10^{4}	2.25×10^{6}
5.0	1.23×10^{2}	3.08×10^{5}	1.06×10^{6}	3.43×10^{4}	2.20×10^{6}
6.0	1.22×10^{2}	3.06×10^{5}	1.05×10^{6}	3.15×10^{4}	2.15×10^{6}
7.0	1.20×10^{2}	3.04×10^{5}	1.04×10^{6}	2.89×10^{4}	2.10×10^{6}
8.0	1.19×10^{2}	3.02×10^{5}	1.03×10^{6}	2.65×10^{4}	2.05×10^{6}
9.0	1.17×10^{2}	3.00×10^{5}	1.02×10^{6}	2.44×10^{4}	2.01×10^{6}
10.0	1.16×10^{2}	2.98×10^{5}	1.01×10^{6}	2.23×10^{4}	1.96×10^{6}
20.0	1.04×10^{2}	2.79×10^{5}	9.54×10^{5}	9.25×10^{3}	1.59×10^{6}
30.0	9.43×10^{a}	2.61×10^{5}	9.0×10^{5}	3.76×10^{3}	1.30×10^{6}

[a]Count rates provided are independent of background. Since background is site dependent, it will need to be independently acquired and subtracted from gross count rates to obtain the triage threshold values.